ACS APPLIED MATERIALS & INTERFACES

Research Article

Cite This: ACS Appl. Mater. Interfaces 2019, 11, 1917−1923

www.acsami.org

Ratiometric Photoacoustic Nanoprobe for Bioimaging of Cu^{2+}

Sheng Wang,[†,‡] Guocan Yu,[‡] Ying Ma,[‡] Zhen Yang,[‡] Yi Liu,[*,§] Jing Wang,[*,†] and Xiaoyuan Chen[*,‡]

[†]Department of Nuclear Medicine, Xijing Hospital, Fourth Military Medical University, Xi'an 710032, China

[‡]Laboratory of Molecular Imaging and Nanomedicine, National Institute of Biomedical Imaging and Bioengineering, National Institutes of Health, Bethesda, Maryland 20892, United States

[§]School of Engineering, China Pharmaceutical University, Nanjing 210009, China

Supporting Information

ABSTRACT: Aberrant copper contents implicate numerous diseases including Alzheimer's disease and Wilson's disease. Conventional copper detection technologies are difficult to offer non-invasive and accurate deep tissue detection of copper. Here, we report a photoacoustic (PA) nanoprobe (NRh-IR-NMs) for ratiometric PA imaging of Cu^{2+}. The nanoprobe consists of a selective Cu^{2+}-responsive probe (NRh) as the indicator and a nonresponsive dye (IR) as the internal reference. In the presence of Cu^{2+}, a selective Cu^{2+}-induced structure change of NRh would take place, resulting in the increase of PA signal intensity increment at 716 nm (ΔPA716). However, the ΔPA834 which attributes to IR shows negligible change. Therefore, the ratiometric PA signal (ΔPA716/ΔPA834) could be used as an indicator for Cu^{2+} detection. This ratiometric PA detection method offers a noninvasive technology with high selectivity and tissue penetration depth, which is a promising tool for deep-tissue detection of Cu^{2+} in living organisms.

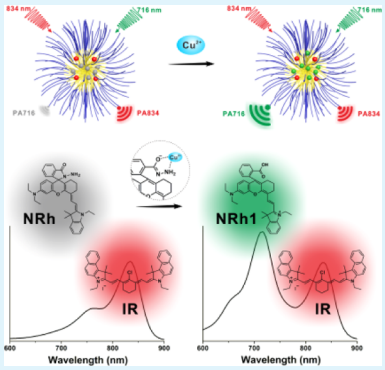

KEYWORDS: *photoacoustic probe, copper ion detection, ratiometric imaging, biosensor, nanotechnology*

1. INTRODUCTION

Photoacoustic (PA) imaging is a newly emerged noninvasive imaging technology.[1−3] By converting pulsed near-infrared (NIR) laser excitation into ultrasonic emission, PA imaging combines the advantages of both optical imaging (high selectivity) and ultrasonic imaging (improved tissue penetration depth).[4−6] Furthermore, ratiometric imaging, which is based on an internal reference approach, can eliminate the environmental effects and thus give more reliable detection result.[7−11] Owing to the merits of ratiometric PA imaging, it has been used as a promising noninvasive technique in a wide range of in vivo bioapplications (e.g. tumor imaging, thrombus imaging, therapy monitoring, pH detection, and enzyme detection).[12−22] However, the application of PA imaging in metal ion detection is still in its infancy.[23−27]

Divalent copper ion (Cu^{2+}) is an important metal ion in living organisms which plays a significant role in many biological processes.[28,29] The copper levels in the human liver and brain are as high as 5 μg per gram of tissue.[30] It has been demonstrated that the aberrant Cu^{2+} level is implicated in numerous severe diseases.[31−33] For example, the increased concentration of Cu^{2+} ions in the brain would promote the aggregation of pathological protein, which is a distinct feature of Alzheimer's disease (AD).[34−36] Additionally, Wilson's disease (WD) is another copper ion-related disease in which copper builds up in various tissues (e.g. liver, brain, kidneys, and cornea) and thus damages these organs and nervous system.[37−39] The liver copper concentration of WD patients is 4.5−16.5-fold higher than that of healthy individuals.[30] Hence, reliable copper detection is of great significance. Conventional copper detection technologies are mainly based on inductively coupled plasma methods.[40−42] Although these technologies enable copper detection with high accuracy, they usually involve invasive procedures that need adequate tissue samples and require tedious procedures. Moreover, these methods can only measure the average copper content of the sample, rather than the copper mapping of the whole tissue. For example, liver biopsy is the gold standard and the most accurate test for the detection of copper contents in liver.[43] However, performing liver biopsy is extremely invasive and is contraindicated in some patients.[44] Furthermore, in the nonrenewable organs (e.g. brain and kidneys) of living organisms, copper contents are difficult to be detected by these techniques. Although various fluorescent probes have enabled detection of metal ions,[45−48] most of them are suboptimal for in vivo applications due to tissue autofluorescence and limited tissue penetration.[49,50] Recently, Li et al. developed acoustogenic probes for in vitro chemoselective imaging of Cu^{2+}.[23] The PA probes show great potential because of their high selectivity and the distinct advantages of PAI. Therefore, the development of more PA probes for in vivo copper detection is highly desirable.

Received: November 15, 2018
Accepted: December 21, 2018
Published: December 21, 2018

DOI: 10.1021/acsami.8b20113
ACS Appl. Mater. Interfaces 2019, 11, 1917−1923

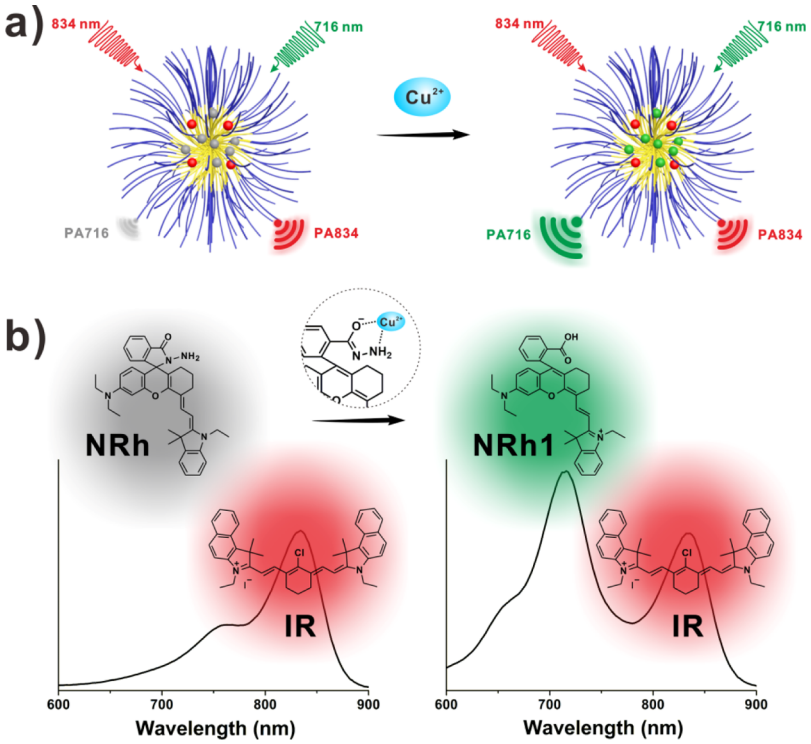

Figure 1. (a) Scheme showing the detection of Cu^{2+} by the PA nanoprobe. (b) Scheme showing the structure and absorption spectra changes of the nanoprobe in the presence of Cu^{2+}.

Herein, we report a ratiometric PA nanoprobe (NRh-IR-NMs) for in vivo deep tissue detection of Cu^{2+}. As shown in Figure 1a, two types of organic probes, selective Cu^{2+}-responsive NRh and nonresponsive IR820 (IR), were encapsulated into nanomicelles (NMs) to form NRh-IR-NMs. In this system, NRh, which can realize selective Cu^{2+}-induced absorbance change, acts as an indicator, whereas IR, whose absorbance is inert to Cu^{2+}, serves as the internal reference. The NRh-IR-NMs have a single absorption peak at about 834 nm (belongs to IR) in the NIR region, resulting in an obvious PA signal at 834 nm (PA834). However, in the presence of Cu^{2+}, a selective Cu^{2+}-induced spirolactam ring opening and further hydrolysis of NRh would take place, thus converting NRh into NRh1. The absorbance of NRh1-IR-NMs at 716 nm (belongs to NRh1) would be increased significantly (Figure 1b), resulting in an amplified PA signal intensity increment at 716 nm (ΔPA716). In contrast, the ΔPA834 of NRh1-IR-NMs shows virtually no change when compared to that of NRh-IR-NMs. Therefore, the ratiometric PA signal (ΔPA716/ΔPA834) could be used for Cu^{2+} detection.

2. EXPERIMENTAL SECTION

2.1. Materials. Poly(ethylene glycol)methyl ether (M_n 5000), ε-caprolactone (CL), and tin(II) 2-ethylhexanoate ($Sn(Oct)_2$) were purchased from Sigma-Aldrich.

2.2. Synthetic Methods. Experimental procedures for the synthesis of NRh, IR, and poly(ethylene glycol)-poly(CL) (PEG-PCL) can be found in the Supporting Information (Schemes S1−S3).

2.3. Cu^{2+}-Induced Response of the NRh. To examine the Cu^{2+}-induced response of the NRh, $CuCl_2$ (10 equiv) aqueous solution was added to 10 μM NRh in the MeOH solution (1 equiv). The mixture was vigorously stirred for 15 min, and the absorption spectra of the solution were measured.

2.4. Preparation and Characterization of the NRh-IR-NMs. NRh (0.470 mg, 0.8 μmol), IR (29.56 μg, 0.04 μmol), and PEG-PCL (4 mg) were dissolved in 500 μL of tetrahydrofuran (THF). Then, 2 mL of pure water was added into the solution under sonication. The THF was then evaporated under reduced pressure at room temperature.

The effective particle diameter and colloidal stability of the NRh-IR-NMs were determined by dynamic light scattering (DLS) (SZ-100 nano particle analyzer, HORIBA Scientific, USA) at room temperature (n = 3). NIR absorption spectra of the samples were measured by a Genesys 10S UV−vis−NIR spectrophotometer (Thermo Scientific, Waltham, MA) (n = 3). In vitro PA imaging of the samples was measured on a Vevo 2100 LAZR system (VisualSonics, Inc., New York) (n = 3). PA signals were acquired within the range of 680−900 nm.

2.5. Cu^{2+}-Induced Response of the NRh-IR-NMs. The aqueous solution of NRh-IR-NMs (NRh concentration: 0.2 mM) was incubated with Cu^{2+} (or other metal ions) aqueous solution (2 mM) at room temperature for different periods of time. Then, the absorption spectra and PA signals of the solutions were measured as mentioned above (n = 3).

2.6. In Vitro Cell Experiments. The in vitro cell cytotoxicity of NRh-IR-NMs was assessed on HeLa cells, which was purchased from American Type Culture Collection (ATCC). HeLa cells were seeded into 96-well plates and incubated at 37 °C for 24 h. Then, the samples were added into each well for an additional 24 h of incubation. Afterward, the relative cell viabilities were measured by the methyl thiazolyl tetrazolium (MTT) assay (n = 5).

2.7. In Vivo PA Imaging. All animal experiments were performed under a National Institutes of Health Animal Care and Use Committee (NIHACUC)-approved protocol. A total of 50 μL (2 mg mL^{-1}) of NRh-IR-NM aqueous solution and different Cu^{2+} solutions were subcutaneously injected into the thigh of living mice (Harlan, Indianapolis, IN). At 2 h postinjection, the in vivo PA imaging was performed on a Vevo 2100 LAZR system (VisualSonics Inc. New York, NY) equipped with a 40 MHz, 256-element linear array transducer (n = 3).

3. RESULTS AND DISCUSSION

3.1. Characterization of NRh and IR. The NRh molecule was synthesized as shown in Scheme S1 (Supporting

DOI: 10.1021/acsami.8b20113
ACS Appl. Mater. Interfaces 2019, 11, 1917−1923

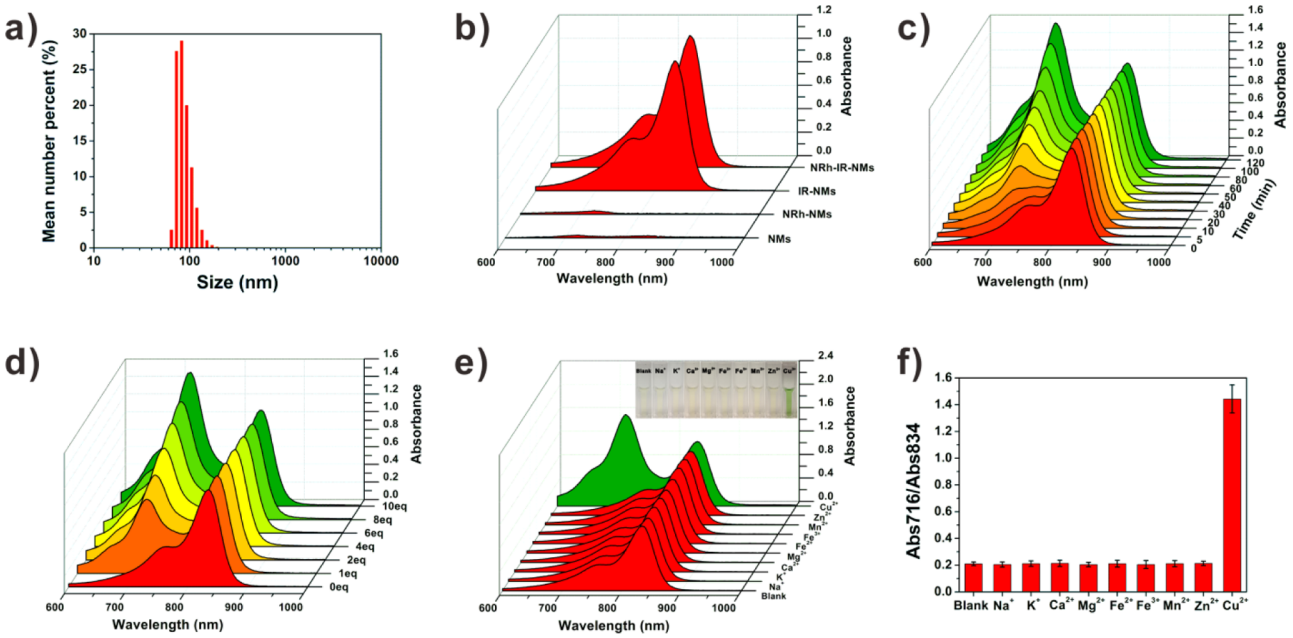

Figure 2. (a) Effective particle diameter of the NRh-IR-NMs. (b) Absorption spectra of NMs, NRh-NMs, IR-NMs, and NRh-IR-NMs. (c) Time-dependent changes in absorption spectra of NRh-IR-NM solution upon the addition of Cu^{2+} solution (10 equiv). (d) Absorption spectra changes of the NRh-IR-NM solutions upon addition of different amounts of Cu^{2+} solution. (e) Absorption spectra and color (inset) changes of the NRh-IR-NM solutions upon addition of different metal ions. (f) Changes in the absorbance ratio (Abs716/Abs834) of NRh-IR-NM solutions upon addition of different metal ions (n = 3).

Information).[51−55] Nuclear magnetic resonance (NMR) and liquid chromatography−mass spectrometry (LC−MS) characterizations demonstrated the chemical structure of NRh (Figures S1−S3, Supporting Information). To examine the Cu^{2+}-induced response of the NRh (Scheme S4, Supporting Information), excessive Cu^{2+} aqueous solution was added to the NRh solution. The solution color turned to green rapidly, and the absorbance at 600−750 nm increased significantly, demonstrating the conversion from NRh into NRh1 (Figure S4, Supporting Information). The LC−MS spectra further confirmed the Cu^{2+}-induced structure change of NRh (Figure S5, Supporting Information). Then, the IR molecule was synthesized according to literature (Scheme S2, Supporting Information).[56] NMR spectra confirmed the successful synthesis of IR (Figures S6 and S7, Supporting Information). As shown in the absorption spectra (Figure S8, Supporting Information), IR molecules have a single absorption peak at about 834 nm. In the presence of Cu^{2+}, the IR did not show any absorbance change in the NIR region, indicating its inertness to Cu^{2+}. Furthermore, the presence of IR would not affect the reaction between NRh and Cu^{2+} (Figure S9, Supporting Information); thus, IR can be used as the internal reference of the ratiometric PA probe.

3.2. Preparation and Characterization of NRh-IR-NMs. An amphiphilic diblock copolymer, PEG-PCL, was synthesized by ring-opening polymerization of CL to prepare the NMs (Scheme S3 and Figure S10, Supporting Information). The two small molecular probes at the NRh/IR molar ratio of 20:1 were encapsulated into PEG-PCL-based NMs to obtain NRh-IR-NMs. The hydrodynamic diameter of NRh-IR-NMs was measured to be 84.2 ± 16.5 nm by DLS (Figure 2a). Furthermore, the NRh-IR-NMs showed good colloidal stability for 7 days (Figure S11, Supporting Information). The nanosized diameter and good colloidal stability of the NRh-IR-NMs made them suitable for in vivo bioapplication. Then, NIR absorption spectra of blank NMs and different probe-loaded NMs were measured. As shown in Figure 2b, both blank NMs and NRh-NMs showed no obvious absorbance in the NIR region; however, IR-NMs and NRh-IR-NMs showed a single characteristic absorption peak of IR at 834 nm.

3.3. Detecting Cu^{2+} in Vitro. To examine Cu^{2+} response of the NRh-IR-NMs, the absorption spectra of the NRh-IR-NM aqueous solutions incubated with different concentrations of Cu^{2+} were measured. The absorption spectra of blank NM aqueous solution showed little change upon addition of Cu^{2+}, indicating non-response of blank NMs (Figure S12, Supporting Information). However, upon the addition of Cu^{2+}, the absorbance at 716 nm (Abs716) of the NRh-IR-NM solution increased gradually, indicating the reaction between NRh molecules and Cu^{2+}. Different from NRh, IR molecules are inert to Cu^{2+}, thus the absorbance at 834 nm (Abs834) of NRh-IR-NMs showed no appreciable change (Figure 2c). As a result, the ratio of Abs716 to Abs834 (Abs716/Abs834) increased over time. As shown in Figure S13 (Supporting Information), after 120 min of incubation with Cu^{2+}, the value of Abs716/Abs834 increased to 1.407, which is about 7-fold higher than its initial value. Moreover, the Cu^{2+} concentration-dependent changes in the absorption spectra of NRh-IR-NMs also gave a significant change of Abs716/Abs834 (Figures 2d and S14, Supporting Information). Indeed, the sensing rate of NRh-IR-NMs in the aqueous environment is relatively low because of the hydrophobicity of NRh. However, it has been reported that WD and AD patients suffer from persistent copper excess in major organs. Therefore, the slow sensing rate will not affect the application potential of the nanoprobe in these diseases. Next, the selectivity of NRh-IR-NMs was investigated. Various metal ions were selected as control groups. As shown in Figure 2e,f, only Cu^{2+}-induced prominent changes in solution color, absorption spectra, and Abs716/Abs834, whereas negligible

DOI: 10.1021/acsami.8b20113
ACS Appl. Mater. Interfaces 2019, 11, 1917−1923

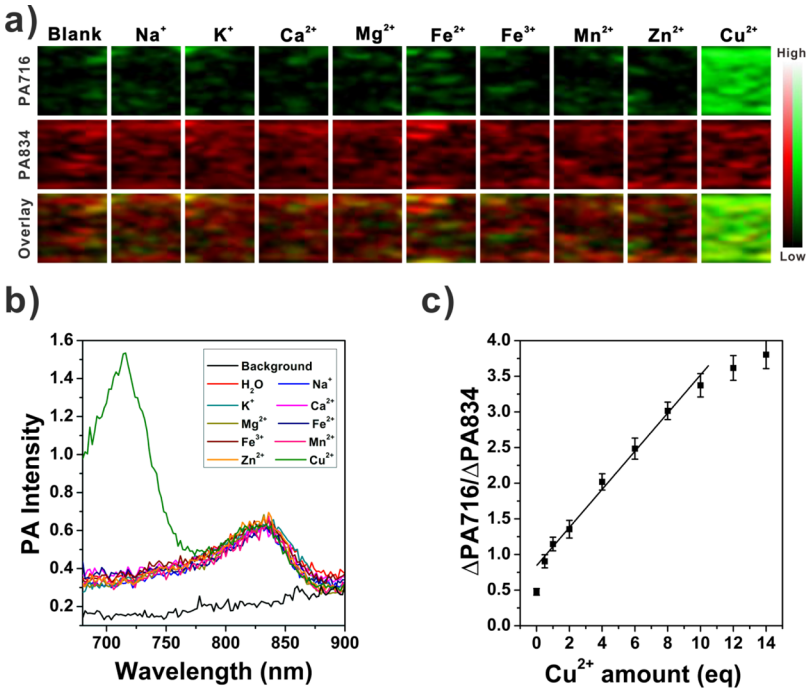

Figure 3. In vitro PA images (a) and PA spectra (b) of the NRh-IR-NM aqueous solution with the addition of pure water or various metal ion solutions. (c) ΔPA716/ΔPA834 of the NRh-IR-NM solution as a function of Cu^{2+} concentration (n = 3).

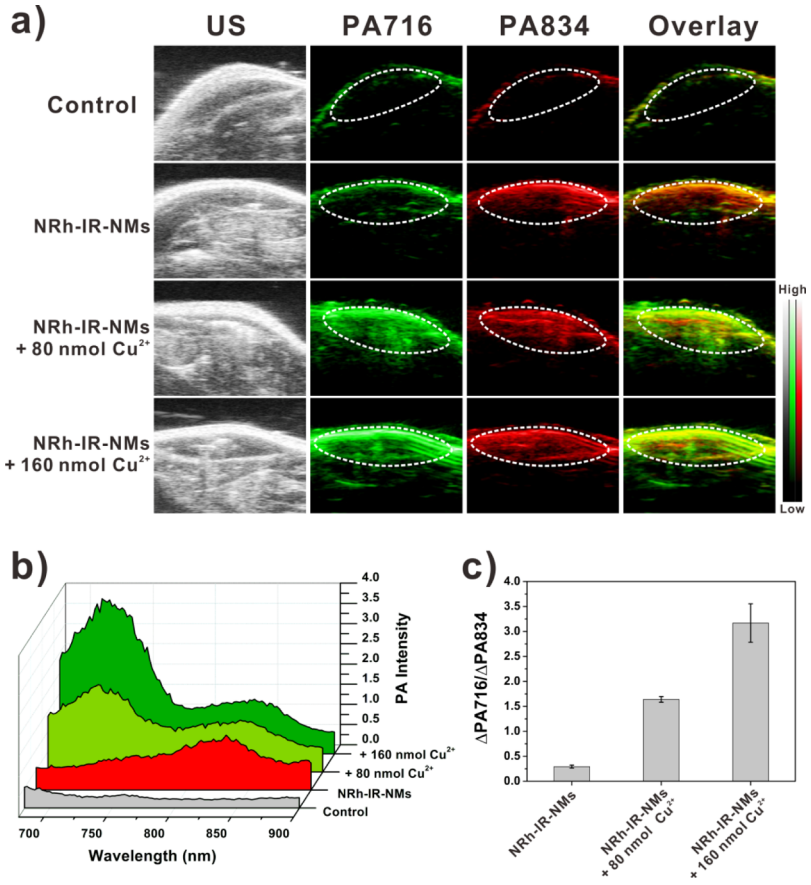

Figure 4. (a) PA images of living mice after subcutaneous administration of saline and NRh-IR-NM solution with or without Cu^{2+}. (b) PA spectra of the region of interest (ROI) in (a). (c) Ratiometric PA signals (ΔPA716/ΔPA834) based on data in (b).

changes were observed in all the control groups, demonstrating great selectivity of the NRh-IR-NMs.

Considering the significant Cu^{2+}-induced absorption change in the NIR region, we further measured the PA properties of

DOI: 10.1021/acsami.8b20113
ACS Appl. Mater. Interfaces 2019, 11, 1917−1923

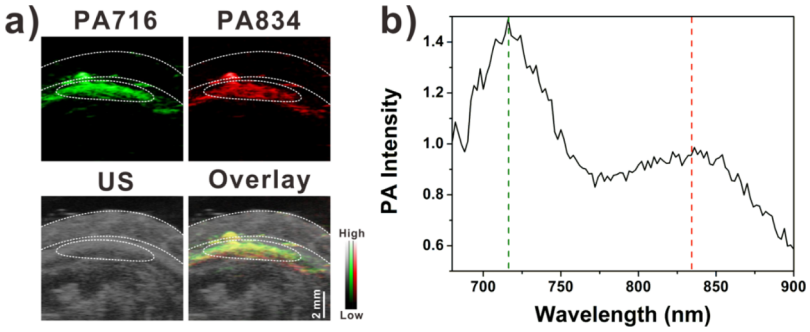

Figure 5. (a) PA images of living mice after subcutaneous administration of NRh-IR-NM solution with Cu^{2+} (covered by 2 mm pork tissue). (b) PA spectrum of ROI in (a).

NRh-IR-NMs in vitro. As shown in Figure 3a,b, compared to the background, the NRh-IR-NM aqueous solution showed an obvious ΔPA834 and a relatively low ΔPA716, resulting in a very low ΔPA716/ΔPA834 (≈0.5). However, in the presence of Cu^{2+}, as expected, the ΔPA834 of the NRh1-IR-NMs showed no prominent change, whereas the ΔPA716 increased significantly, resulting in an increased ΔPA716/ΔPA834 (≈3.4), which is about 7-fold higher than that of NRh-IR-NMs (Figures S15 and S16, Supporting Information). The calculated ΔPA716/ΔPA834 was higher than Abs716/Abs834, which may be because the different photothermal conversion efficiencies between NRh and IR. Furthermore, the changes of ΔPA716/ΔPA834 showed Cu^{2+} concentration dependence in the range of 0.5−10.0 equiv (Figure 3c). In contrast, with the addition of other metal ions, the PA intensities and the ΔPA716/ΔPA834 of the solutions showed no changes (Figures 3 and S15 and S16, Supporting Information), which further demonstrated the selectivity of the PA nanoprobe.

3.4. Cytotoxicity. To assess the cytotoxicity and biocompatibility of NRh-IR-NMs, HeLa cells were incubated with NRh-IR-NMs at different concentrations (0−400 mg L^{-1}). After 24 h of incubation, the cell viabilities were investigated by the MTT assay. As shown in Figure S17 (Supporting Information), even at a high concentration (400 mg L^{-1}) of NRh-IR-NMs, the cell viability was still more than 90%, indicating the negligible cytotoxicity of the NRh-IR-NMs.

3.5. In Vivo PA Imaging of Cu^{2+}. In vivo PA imaging of Cu^{2+} was tested by subcutaneous administration of Cu^{2+} solution and NRh-IR-NMs in the thigh of living mice. At 2 h postinjection, the PA spectra were monitored. For the mice treated with saline (control group), the background PA signals at both 716 and 834 nm were very low (Figure 4a,b). After the injection of NRh-IR-NMs, obvious PA834 was observed, whereas PA716 showed negligible change (Figure S18, Supporting Information). The calculated ΔPA716/ΔPA834, thus, has a relatively low value (about 0.3, Figure 4c). However, for the mice injected with Cu^{2+}, increased PA716 can be clearly detected, indicating the reaction between NRh molecules and Cu^{2+}. As a result, the ΔPA716/ΔPA834 values of the NRh-IR-NMs/Cu^{2+} groups were much higher than those of the NRh-IR-NM-only group (Figure 4c). Furthermore, the ΔPA716/ΔPA834 value within the region is dependent on the dosage of the administrated Cu^{2+}. To investigate the potential of NRh-IR-NMs for deep-tissue application, as a proof-of-concept experiment, Cu^{2+} solution and NRh-IR-NMs were injected subcutaneously into the thigh of living mice. Then, the thigh was covered by a 2 mm pork tissue and observed by PA imaging. As shown in Figure 5, PA signals in the deep region (depth at 2.0−4.0 mm) were clearly observed. All of these results manifest the potential of NRh-IR-NMs for deep tissue detection of Cu^{2+} in living mice. Based on the size and surface modification of the nanoprobe, we believe that the NRh-IR-NMs are suitable for intravenous injection and the intravenously injected nanoprobe will be mainly distributed in liver. Considering high copper concentration in the liver of WD patients, we anticipate that the NRh-IR-NMs will be useful for liver copper detection in a WD model.

4. CONCLUSIONS

In summary, a noninvasive strategy based on the ratiometric PA nanoprobe (NRh-IR-NMs) was developed for in vivo detection of Cu^{2+} in living mice. In this system, two small molecular NIR probes, NRh as a Cu^{2+}-responsive indicator and IR as a Cu^{2+}-inert internal reference, were encapsulated into NMs, simultaneously. In the presence of Cu^{2+}, a selective Cu^{2+}-induced reaction would take place and thus lead to changes of PA intensities, and then ratiometric PA imaging can be used to detect the Cu^{2+} in vivo. This ratiometric PA detection method is a noninvasive technology with high selectivity and improved tissue penetration depth, which may be a great tool for Cu^{2+} detection in living organisms. Considering the critical role of Cu^{2+} for major neuronal functions, the ratiometric PA nanoprobe has great potential for detection of Cu^{2+} in numerous diseases such as AD and WD.

■ ASSOCIATED CONTENT

Supporting Information

The Supporting Information is available free of charge on the ACS Publications website at DOI: 10.1021/acsami.8b20113.

Synthesis process and NMR characterization of NRh, IR, and PEG-PCL. UV−vis−NIR absorption spectra and PA spectra of different samples (PDF)

■ AUTHOR INFORMATION

Corresponding Authors

*E-mail: yiliu@cpu.edu.cn (Y.L.).
*E-mail: wangjing@fmmu.edu.cn (J.W.).
*E-mail: shawn.chen@nih.gov (X.C.).

ORCID

Zhen Yang: 0000-0003-4056-0347
Yi Liu: 0000-0001-5008-1097
Xiaoyuan Chen: 0000-0002-9622-0870

Notes

The authors declare no competing financial interest.

DOI: 10.1021/acsami.8b20113
ACS Appl. Mater. Interfaces 2019, 11, 1917−1923

ACKNOWLEDGMENTS

This work was supported by the Shaanxi Science & Technology Coordination & Innovation Project (2016KTCQ03-09), The International Cooperation Program of Xijing Hospital (XJZT15G01), the National Science Foundation of China (81601531, 81771900), the National Science Foundation of Jiangsu Province (BK20160755), the "Double First-Class" University project (CPU2018GY24), and the Intramural Research Program (IRP) of the National Institute of Biomedical Imaging and Bioengineering (NIBIB), National Institutes of Health (NIH).

REFERENCES

(1) Kim, C.; Favazza, C.; Wang, L. V. In Vivo Photoacoustic Tomography of Chemicals: High-Resolution Functional and Molecular Optical Imaging at New Depths. *Chem. Rev.* **2010**, *110*, 2756−2782.

(2) Nie, L.; Chen, X. Structural and Functional Photoacoustic Molecular Tomography Aided by Emerging Contrast Agents. *Chem. Soc. Rev.* **2014**, *43*, 7132−7170.

(3) Weber, J.; Beard, P. C.; Bohndiek, S. E. Contrast Agents for Molecular Photoacoustic Imaging. *Nat. Methods* **2016**, *13*, 639−650.

(4) Wang, S.; Lin, J.; Wang, T.; Chen, X.; Huang, P. Recent Advances in Photoacoustic Imaging for Deep-Tissue Biomedical Applications. *Theranostics* **2016**, *6*, 2394−2413.

(5) Liu, Y.; Nie, L.; Chen, X. Photoacoustic Molecular Imaging: From Multiscale Biomedical Applications Towards Early-Stage Theranostics. *Trends Biotechnol.* **2016**, *34*, 420−433.

(6) Jiang, Y.; Pu, K. Advanced Photoacoustic Imaging Applications of Near-Infrared Absorbing Organic Nanoparticles. *Small* **2017**, *13*, 1700710.

(7) Zhuang, Y.; Xu, Q.; Huang, F.; Gao, P.; Zhao, Z.; Lou, X.; Xia, F. Ratiometric Fluorescent Bioprobe for Highly Reproducible Detection of Telomerase in Bloody Urines of Bladder Cancer Patients. *ACS Sens.* **2016**, *1*, 572−578.

(8) Miao, Q.; Lyu, Y.; Ding, D.; Pu, K. Semiconducting Oligomer Nanoparticles as an Activatable Photoacoustic Probe with Amplified Brightness for In Vivo Imaging of pH. *Adv. Mater.* **2016**, *28*, 3662−3668.

(9) Wu, L.; Wu, I.-C.; DuFort, C. C.; Carlson, M. A.; Wu, X.; Chen, L.; Kuo, C.-T.; Qin, Y.; Yu, J.; Hingorani, S. R.; Chiu, D. T. Photostable Ratiometric Pdot Probe for In Vitro and In Vivo Imaging of Hypochlorous Acid. *J. Am. Chem. Soc.* **2017**, *139*, 6911−6918.

(10) Yin, C.; Zhen, X.; Fan, Q.; Huang, W.; Pu, K. Degradable Semiconducting Oligomer Amphiphile for Ratiometric Photoacoustic Imaging of Hypochlorite. *ACS Nano* **2017**, *11*, 4174−4182.

(11) Huang, X.; Song, J.; Yung, B. C.; Huang, X.; Xiong, Y. Ratiometric Optical Nanoprobes Enable Accurate Molecular Detection and Imaging. *Chem. Soc. Rev.* **2018**, *47*, 2873−2920.

(12) Pu, K.; Shuhendler, A. J.; Jokerst, J. V.; Mei, J.; Gambhir, S. S.; Bao, Z.; Rao, J. Semiconducting Polymer Nanoparticles as Photoacoustic Molecular Imaging Probes in Living Mice. *Nat. Nanotechnol.* **2014**, *9*, 233−239.

(13) Yang, K.; Zhu, L.; Nie, L.; Sun, X.; Cheng, L.; Wu, C.; Niu, G.; Chen, X.; Liu, Z. Visualization of Protease Activity In Vivo Using an Activatable Photo-Acoustic Imaging Probe Based on CuS Nanoparticles. *Theranostics* **2014**, *4*, 134−141.

(14) Fan, Q.; Cheng, K.; Yang, Z.; Zhang, R.; Yang, M.; Hu, X.; Ma, X.; Bu, L.; Lu, X.; Xiong, X.; Huang, H.; Cheng, Z. Perylene-Diimide-Based Nanoparticles as Highly Efficient Photoacoustic Agents for Deep Brain Tumor Imaging in Living Mice. *Adv. Mater.* **2015**, *27*, 843−847.

(15) Pu, K.; Mei, J.; Jokerst, J. V.; Hong, G.; Antaris, A. L.; Chattopadhyay, N.; Shuhendler, A. J.; Kurosawa, T.; Zhou, Y.; Gambhir, S. S.; Bao, Z.; Rao, J. Diketopyrrolopyrrole-Based Semiconducting Polymer Nanoparticles for In Vivo Photoacoustic Imaging. *Adv. Mater.* **2015**, *27*, 5184−5190.

(16) Ho, I.-T.; Sessler, J. L.; Gambhir, S. S.; Jokerst, J. V. Parts Per Billion Detection of Uranium with a Porphyrinoid-Containing Nanoparticle and In Vivo Photoacoustic Imaging. *Analyst* **2015**, *140*, 3731−3737.

(17) Lyu, Y.; Fang, Y.; Miao, Q.; Zhen, X.; Ding, D.; Pu, K. Intraparticle Molecular Orbital Engineering of Semiconducting Polymer Nanoparticles as Amplified Theranostics for In Vivo Photoacoustic Imaging and Photothermal Therapy. *ACS Nano* **2016**, *10*, 4472−4481.

(18) Yang, Z.; Song, J.; Dai, Y.; Chen, J.; Wang, F.; Lin, L.; Liu, Y.; Zhang, F.; Yu, G.; Zhou, Z.; Fan, W.; Huang, W.; Fan, Q.; Chen, X. Self-Assembly of Semiconducting-Plasmonic Gold Nanoparticles with Enhanced Optical Property for Photoacoustic Imaging and Photothermal Therapy. *Theranostics* **2017**, *7*, 2177−2185.

(19) Wang, S.; Lin, J.; Wang, Z.; Zhou, Z.; Bai, R.; Lu, N.; Liu, Y.; Fu, X.; Jacobson, O.; Fan, W.; Qu, J.; Chen, S.; Wang, T.; Huang, P.; Chen, X. Core-Satellite Polydopamine-Gadolinium-Metallofullerene Nanotheranostics for Multimodal Imaging Guided Combination Cancer Therapy. *Adv. Mater.* **2017**, *29*, 1701013.

(20) Cui, C.; Yang, Z.; Hu, X.; Wu, J.; Shou, K.; Ma, H.; Jian, C.; Zhao, Y.; Qi, B.; Hu, X.; Yu, A.; Fan, Q. Organic Semiconducting Nanoparticles as Efficient Photoacoustic Agents for Lightening Early Thrombus and Monitoring Thrombolysis in Living Mice. *ACS Nano* **2017**, *11*, 3298−3310.

(21) Roberts, S.; Andreou, C.; Choi, C.; Donabedian, P.; Jayaraman, M.; Pratt, E. C.; Tang, J.; Pérez-Medina, C.; Jason de la Cruz, M.; Mulder, W. J. M.; Grimm, J.; Kircher, M.; Reiner, T. Sonophore-Enhanced Nanoemulsions for Optoacoustic Imaging of Cancer. *Chem. Sci.* **2018**, *9*, 5646−5657.

(22) Kim, T.; Zhang, Q.; Li, J.; Zhang, L.; Jokerst, J. V. A Gold/Silver Hybrid Nanoparticle for Treatment and Photoacoustic Imaging of Bacterial Infection. *ACS Nano* **2018**, *12*, 5615−5625.

(23) Li, H.; Zhang, P.; Smaga, L. P.; Hoffman, R. A.; Chan, J. Photoacoustic Probes for Ratiometric Imaging of Copper(II). *J. Am. Chem. Soc.* **2015**, *137*, 15628−15631.

(24) Cash, K. J.; Li, C.; Xia, J.; Wang, L. V.; Clark, H. A. Optical Drug Monitoring: Photoacoustic Imaging of Nanosensors to Monitor Therapeutic Lithium In Vivo. *ACS Nano* **2015**, *9*, 1692−1698.

(25) Mishra, A.; Jiang, Y.; Roberts, S.; Ntziachristos, V.; Westmeyer, G. G. Near-Infrared Photoacoustic Imaging Probe Responsive to Calcium. *Anal. Chem.* **2016**, *88*, 10785−10789.

(26) Liu, Y.; Wang, S.; Ma, Y.; Lin, J.; Wang, H.-Y.; Gu, Y.; Chen, X.; Huang, P. Ratiometric Photoacoustic Molecular Imaging for Methylmercury Detection in Living Subjects. *Adv. Mater.* **2017**, *29*, 1606129.

(27) Roberts, S.; Seeger, M.; Jiang, Y.; Mishra, A.; Sigmund, F.; Stelzl, A.; Lauri, A.; Symvoulidis, P.; Rolbieski, H.; Preller, M.; Deán-Ben, X. L.; Razansky, D.; Orschmann, T.; Desbordes, S. C.; Vetschera, P.; Bach, T.; Ntziachristos, V.; Westmeyer, G. G. Calcium Sensor for Photoacoustic Imaging. *J. Am. Chem. Soc.* **2018**, *140*, 2718−2721.

(28) Desai, V.; Kaler, S. G. Role of Copper in Human Neurological Disorders. *Am. J. Clin. Nutr.* **2008**, *88*, 855S−858S.

(29) Manto, M. Abnormal Copper Homeostasis: Mechanisms and Roles in Neurodegeneration. *Toxics* **2014**, *2*, 327−345.

(30) Giampietro, R.; Spinelli, F.; Contino, M.; Colabufo, N. A. The Pivotal Role of Copper in Neurodegeneration: A New Strategy for the Therapy of Disorders. *Mol. Pharmaceutics* **2018**, *15*, 808−820.

(31) Squitti, R.; Lupoi, D.; Pasqualetti, P.; Dal Forno, G.; Vernieri, F.; Chiovenda, P.; Rossi, L.; Cortesi, M.; Cassetta, E.; Rossini, P. M. Elevation of Serum Copper Levels in Alzheimer's Disease. *Neurology* **2002**, *59*, 1153−1161.

(32) Kitzberger, R.; Madl, C.; Ferenci, P. Wilson Disease. *Metab. Brain Dis.* **2005**, *20*, 295−302.

(33) Madsen, E.; Gitlin, J. D. Copper and Iron Disorders of the Brain. *Annu. Rev. Neurosci.* **2007**, *30*, 317−337.

(34) Bush, A. I. The Metallobiology of Alzheimer's Disease. *Trends Neurosci.* **2003**, *26*, 207−214.

(35) Tiiman, A.; Palumaa, P.; Tõugu, V. The Missing Link in the Amyloid Cascade of Alzheimer's Disease - Metal Ions. *Neurochem. Int.* **2013**, *62*, 367−378.

DOI: 10.1021/acsami.8b20113
ACS Appl. Mater. Interfaces 2019, 11, 1917−1923

(36) Cui, Z.; Bu, W.; Fan, W.; Zhang, J.; Ni, D.; Liu, Y.; Wang, J.; Liu, J.; Yao, Z.; Shi, J. Sensitive Imaging and Effective Capture of Cu^{2+}: Towards Highly Efficient Theranostics of Alzheimer's Disease. *Biomaterials* **2016**, *104*, 158−167.
(37) Cox, D. W.; Moore, S. D. P. Copper Transporting P-Type ATPases and Human Disease. *J. Bioenerg. Biomembr.* **2002**, *34*, 333−338.
(38) Ala, A.; Walker, A. P.; Ashkan, K.; Dooley, J. S.; Schilsky, M. L. Wilson's Disease. *Lancet* **2007**, *369*, 397−408.
(39) Behari, M.; Pardasani, V. Genetics of Wilsons Disease. *Park. Relat. Disord.* **2010**, *16*, 639−644.
(40) Ng, K. C.; Garner, T. J. Microwave-Induced Plasma Atomic Absorption Spectrometry with Solution Nebulization and Desolvation-Condensation. *Appl. Spectrosc.* **1993**, *47*, 241−243.
(41) Bersier, P. M.; Howell, J.; Bruntlett, C. Tutorial Review. Advanced Electroanalytical Techniques Versus Atomic Absorption Spectrometry, Inductively Coupled Plasma Atomic Emission Spectrometry and Inductively Coupled Plasma Mass Spectrometry in Environmental Analysis. *Analyst* **1994**, *119*, 219−232.
(42) Richardson, S. D. Mass Spectrometry in Environmental Sciences. *Chem. Rev.* **2001**, *101*, 211−254.
(43) Ludwig, J.; Moyer, T. P.; Rakela, J. The Liver Biopsy Diagnosis of Wilson's Disease:Methods in Pathology. *Am. J. Clin. Pathol.* **1994**, *102*, 443−446.
(44) Mak, C. M.; Lam, C.-W. Diagnosis of Wilson's Disease: A Comprehensive Review. *Crit. Rev. Clin. Lab. Sci.* **2008**, *45*, 263−290.
(45) Zhao, Q.; Li, F.; Huang, C. Phosphorescent Chemosensors Based on Heavy-Metal Complexes. *Chem. Soc. Rev.* **2010**, *39*, 3007−3030.
(46) Yang, Y.; Zhao, Q.; Feng, W.; Li, F. Luminescent Chemodosimeters for Bioimaging. *Chem. Rev.* **2013**, *113*, 192−270.
(47) Yang, H.; Han, C.; Zhu, X.; Liu, Y.; Zhang, K. Y.; Liu, S.; Zhao, Q.; Li, F.; Huang, W. Upconversion Luminescent Chemodosimeter Based on NIR Organic Dye for Monitoring Methylmercury In Vivo. *Adv. Funct. Mater.* **2016**, *26*, 1945−1953.
(48) Ge, Y.; Ji, R.; Shen, S.; Cao, X.; Li, F. A Ratiometric Fluorescent Probe for Sensing Cu^{2+} Based on New Imidazo [1,5-a] Pyridine Fluorescent Dye. *Sens. Actuators, B* **2017**, *245*, 875−881.
(49) Leblond, F.; Davis, S. C.; Valdés, P. A.; Pogue, B. W. Pre-Clinical Whole-Body Fluorescence Imaging: Review of Instruments, Methods and Applications. *J. Photochem. Photobiol., B* **2010**, *98*, 77−94.
(50) Chen, Q.; Liu, X.; Chen, J.; Zeng, J.; Cheng, Z.; Liu, Z. A Self-Assembled Albumin-Based Nanoprobe for In Vivo Ratiometric Photoacoustic pH Imaging. *Adv. Mater.* **2015**, *27*, 6820−6827.
(51) Yuan, L.; Lin, W.; Yang, Y.; Chen, H. A Unique Class of Near-Infrared Functional Fluorescent Dyes with Carboxylic-Acid-Modulated Fluorescence On/Off Switching: Rational Design, Synthesis, Optical Properties, Theoretical Calculations, and Applications for Fluorescence Imaging in Living Animals. *J. Am. Chem. Soc.* **2012**, *134*, 1200−1211.
(52) Yuan, L.; Lin, W.; Zheng, K.; He, L.; Huang, W. Far-Red to Near Infrared Analyte-Responsive Fluorescent Probes Based on Organic Fluorophore Platforms for Fluorescence Imaging. *Chem. Soc. Rev.* **2013**, *42*, 622−661.
(53) Liu, Y.; Su, Q.; Chen, M.; Dong, Y.; Shi, Y.; Feng, W.; Wu, Z.-Y.; Li, F. Near-Infrared Upconversion Chemodosimeter for In Vivo Detection of Cu^{2+} in Wilson Disease. *Adv. Mater.* **2016**, *28*, 6625−6630.
(54) Liu, Y.; Su, Q.; Zou, X.; Chen, M.; Feng, W.; Shi, Y.; Li, F. Near-Infrared In Vivo Bioimaging Using a Molecular Upconversion Probe. *Chem. Commun.* **2016**, *52*, 7466−7469.
(55) Chen, H.; Dong, B.; Tang, Y.; Lin, W. A Unique "Integration" Strategy for the Rational Design of Optically Tunable Near-Infrared Fluorophores. *Acc. Chem. Res.* **2017**, *50*, 1410−1422.
(56) Liu, Y.; Chen, M.; Cao, T.; Sun, Y.; Li, C.; Liu, Q.; Yang, T.; Yao, L.; Feng, W.; Li, F. A Cyanine-Modified Nanosystem for In Vivo Upconversion Luminescence Bioimaging of Methylmercury. *J. Am. Chem. Soc.* **2013**, *135*, 9869−9876.

DOI: 10.1021/acsami.8b20113
ACS Appl. Mater. Interfaces 2019, 11, 1917−1923